

Effect of Ligand Structure on MnO Nanoparticles for Enhanced T_1 Magnetic Resonance Imaging of Inflammatory Macrophages

Joseph Park,^[a] Doyeon Bang,^[a] Eunjung Kim,^[a] Jaemoon Yang,^[b] Eun-Kyung Lim,^[a] Jihye Choi,^[a] Byunghoon Kang,^[a] Jin-Suck Suh,^[b] Hyo Seon Park,^[c] Yong-Min Huh,^{*[b]} and Seungjoo Haam^{*[a]}

Keywords: Nanomaterials / Nanoparticles / Imaging agents / Magnetic resonance imaging / Ligand effects / Manganese

Carboxymethyl-dextran (CM-dextran) replaced the hydrophobic oleylamine ligands on the surfaces of MnO nanoparticles, rendering them highly water-soluble by allowing direct contact with excited water protons. Solution MRI studies of the two types of nanoparticles, exchanged and bilayered, with different core sizes have shown that the exchanged li-

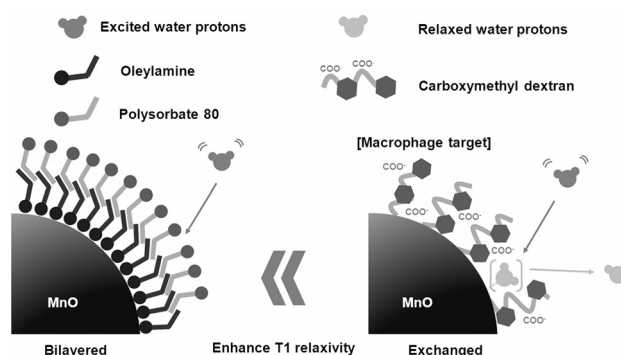
gand structure exhibits significantly enhanced longitudinal relaxation. The modification with dextran converted the nanoparticles into effective T_1 MRI contrast agents, as well as promoting strong interactions with macrophages. Thus, it is a potential MR contrast agent for visualizing inflammatory macrophages.

Introduction

Nanomaterials with surface molecular layers are of great interest for their use in biomedical imaging agents and drug/gene delivery applications. The surface properties can be engineered and improved by controlling their nanoscale lengths, patterns and structures.^[1–4] For example, the lengths of coating molecules on superparamagnetic iron oxide nanoparticles (SPIO) can be optimized to yield high T_2 relaxivity even if their iron oxide core sizes are similar.^[2] The surface patterns of gold nanoparticles (striped AuNP) play a critical role in penetrating the plasma membranes of cells delivering DNA, and AuNPs bearing random ligand configurations are limited.^[4] Likewise, there have been many reports in the literature dealing with surface structures to expedite metal-ion interactions with excited water molecules. In the case of typically used bilayer structures, a metal core with a thick hydrophobic hydrocarbon inner coating may potentially inhibit water penetration, which may result in a lower spin–lattice effect and explain the relatively low R1 relaxivity.^[5,6] Therefore it is highly important to develop a more water-contactable ligand structure by controlling the nature of the nanomaterial surfaces, creating

sufficient stability for use in the accurate detection of specific diseases without compromising the contrast effect.

Herein, we report on the effect of ligand structure on MnO nanoparticles that can be used as T_1 contrast agents. The facile water access to “exposed” metal ions as a result of ligand exchange and smaller nanoparticles with a high surface-area-to-volume ratio (carboxymethyl-dextran-functionalized MnO nanoparticles, CADMOs) allows for an effectively enhanced T_1 MR contrast agent that can visualize macrophage cells (Scheme 1). Inflammatory macrophages are primary targets for molecular imaging because they play an important role in the development of atherosclerosis, releasing cytokines, reactive oxygen species and proteases that can accelerate damage to normal vessels.^[7–15] To assess the potential of CADMOs as enhanced T_1 contrast agent imaging probes, their MR properties, chemical structure, biocompatibility, in vitro cellular uptake and in vivo imaging efficacy have been evaluated.



Scheme 1. Schematic illustration of the effect of ligand structure on MnO nanoparticles as enhanced T_1 MR imaging contrast agents.

[a] Department of Chemical and Biomolecular Engineering, Yonsei University, Seoul 120-749, Republic of Korea
E-mail: haam@yonsei.ac.kr
Homepage: <http://nbsl.yonsei.ac.kr>

[b] Department of Radiology, Yonsei University, Seoul 120-749, Republic of Korea
E-mail: ymhuh@yuhs.ac

[c] Department of Architectural Engineering, Yonsei University, Seoul 120-749, South Korea

Supporting information for this article is available on the WWW under <http://dx.doi.org/10.1002/ejic.201201026>.

Results and Discussion

Oleylamine-functionalized manganese nanoparticles were synthesized with size monodispersity and a highly crystalline structure by thermal decomposition of manganese oleate complexes, as previously reported.^[16] Transmission electron microscopy (TEM) showed that the synthesized oleylamine-functionalized MnO nanoparticles exhibit a highly monodisperse morphology with average diameters of 7.4 and 17.2 nm (see parts a and c of Figure 1 and Supporting Information, Figure S1). Moreover, the core size and shape of the MnO nanoparticles were well maintained after surface modification with CM-dextran (Figure 1, b,d).^[17] To demonstrate the potential of CM-dextran as a stabilizing material for surface modification and the phase transfer of hydrophobic MnO nanoparticles into the aqueous phase, a control experiment was performed with dextran containing only hydroxy groups. In the absence of carboxy groups on the dextran, as we expected, the MnO nanoparticles could not be stabilized well in buffer solution (Figure 1, e). Furthermore, successful phase transfer from hexane to aqueous solution was observed after surface ligand exchange of oleylamine for CM-dextran (see Figure S2 in the Supporting Information). To better understand the particle distribution, number-weighted size distributions were plotted for CADMO-7 and CADMO-17 (Figure 1, f).

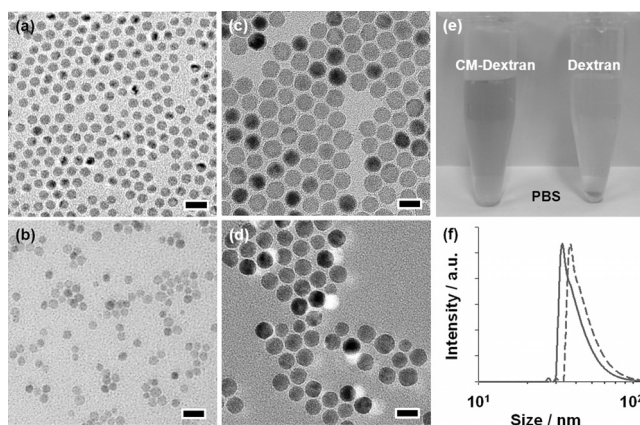


Figure 1. TEM images (all scale bars: 20 nm) of (a) 7 nm MnO in hexane, (b) CADMO-7 in aqueous solution, (c) 17 nm MnO in hexane, (d) CADMO-17 in aqueous solution, (e) photos of the dispersibility of carboxymethyl-dextran (CM-dextran) and dextran-functionalized MnO nanoparticles in phosphate buffer solution (PBS) and (f) size distributions of CADMO-7 (solid line) and CADMO-17 (dotted line).

The powder X-ray diffraction (XRD) data for CADMO-7 indicate that the crystalline peaks match the series of Bragg reflections corresponding to the standard and that the phase-pure cubic rock salt structure of MnO ($a = 4.442 \text{ \AA}$) is maintained after ligand exchange (Figure 2, a). In addition, the particle size, calculated from the Debye–Scherrer equation, is 6.8 nm, which indicates that the powder XRD pattern of CADMO-7 is consistent with pure MnO nanoparticles. The field-dependent magnetization curves for CADMO-7 and CADMO-17 show saturation

magnetization values of 2.96 and 1.82 emu/g, respectively, with no remanence coercivity at zero field showing paramagnetic properties at room temperature (Figure 2, b).

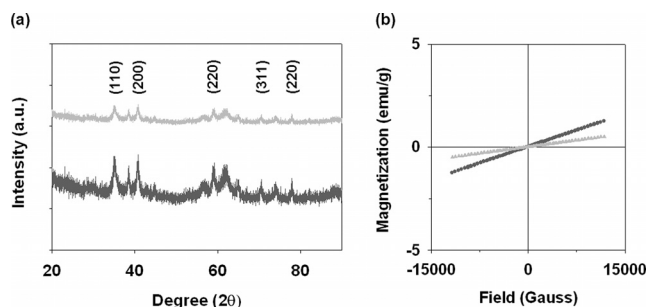


Figure 2. (a) Powder X-ray diffraction pattern and (b) magnetic hysteresis loops analyzed by using a vibrating sample magnetometer for CADMO-7 and CADMO-17.

Excellent dispersion of CADMO-7 and CADMO-17 in aqueous solution over a wide pH range (pH 5–10) with consistent size distributions was confirmed by using dynamic laser scattering analysis (Figure 3). In addition, the pH-dependent ζ -potential data and corresponding isoelectric point (IEP) values (pH IEP = 4.3) were attributed to the presence of the carboxylic groups of CADMO. The acid/base equilibrium favoured the carboxylate anion in the higher pH range (pH > 8) and the ζ potentials of the CADMOs were stabilized at approximately -30 mV , which suggests that all of the carboxy groups exist in the carboxylate anion form. The surface charge was invariant, even when the environmental pH was increased. This robust phase transfer of MnO nanoparticles from an organic to an aqueous physiological environment was attributed to the hydrophilic nature of the CM-dextran chains anchored on the surfaces of the MnO nanoparticles. Specifically, the immobilization of CM-dextran on the inorganic MnO nanoparticles improved their aqueous colloidal stability due to the stabilization effect of the unbound carboxymethyl and hydroxy chains. These unbound chains may partially contribute to the improved dispersion stability by transforming the remaining uncoordinated groups into an ionized form in various pH conditions. In addition, we monitored the stability of CADMOs in various concentrations of fetal bovine serum (25, 50 and 100%) for 3 days. We found that MnO nanoparticles stabilized with carboxymethyl-dextran

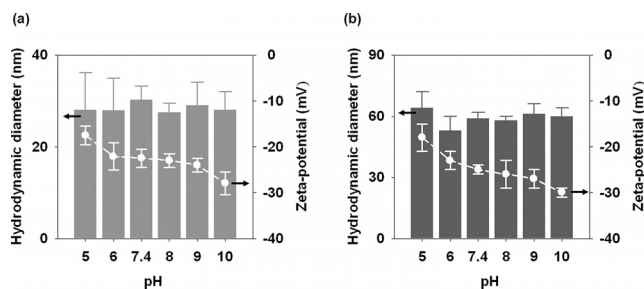


Figure 3. Dynamic light scattering analysis of (a) CADMO-7 and (b) CADMO-17 with evaluation of particle size and ζ potential for various pH conditions.

are stable in the serum for a storage period of around three days. A slight precipitation had appeared after that time, however, no aggregated form was detected. This has been attributed to multiple carboxy groups exhibiting enhanced binding to the surfaces of nanoparticles (see Figure S3 in the Supporting Information).

To validate the potential of the CADMOs as T_1 contrast agents, we acquired T_1 -weighted MR images and measured the relaxation rates as a function of metal concentration using a 1.5T MRI scanner. As a control experiment, we prepared a bilayer structure of MnO nanoparticles (EnMO-7, EnMO-17) that were encapsulated with thick hydrophobic layers (polysorbate80) to inhibit water penetration. CADMO-7 induced the brightest signal enhancement, as shown in the concentration-dependent plot for the T_1 -weighted images (Figure 4, a). The longitudinal relaxivity (r_1) of CADMO-7 ($5.42 \text{ mM}^{-1} \text{ s}^{-1}$) is 49.27, 2.8 times higher than those of EnMO-7 (bilayer structure, $0.12 \text{ mM}^{-1} \text{ s}^{-1}$) and CADMO-17 (large core, $1.91 \text{ mM}^{-1} \text{ s}^{-1}$), respectively. This enhanced relaxivity of CADMO-7 might be due to the increased amount of metal ions exposed to potential surface contact and the use of smaller nanoparticles with a high surface-to-volume (S/V) ratio, which provides greater accessibility and facilitates interactions with the surrounding water molecules (see Figure S4 in the Supporting Information). CADMO-7 shows a 2.42-fold higher S/V ratio compared with CADMO-17 at a given metal-ion concentration. To evaluate the correlation between the S/V ratios and longitudinal relaxivities, we used the Pearson correlation. The Pearson coefficient, calculated from a set of manganese oxide nanoparticles, is 0.96, which indicates a strong correlation between the surface area and the longitudinal relaxivity. A large number of paramagnetic manganese ions exposed on the surface accelerate the spin relaxation process of water protons and consequently shorten the T_1 relaxation time.^[18–21] The r_1 values determined for CADMO-7 are comparable to those of previously reported manganese oxide nanoparticle-based MRI contrast agents (Table 1). Furthermore, manganese oxide nanoparticles

seem to offer additional potential as T_2 negative contrast agents. The T_2 -weighted MR imaging sequences of water-contactable CADMO-7 and CADMO-17 exhibit r_2 coefficients of 31.32 and $11.59 \text{ mM}^{-1} \text{ s}^{-1}$, that is, values that are 18- and 22-fold higher than those of the bilayer structures (EnMO-7: $1.74 \text{ mM}^{-1} \text{ s}^{-1}$; EnMO-17: $0.52 \text{ mM}^{-1} \text{ s}^{-1}$), respectively (Figure 4, b). It can be inferred that the increased T_2 relaxivities of the CADMOs may be due to the surface ligand exchange process being enhanced by the rapid diffusion and exchange of water molecules surrounding the core materials.^[14,22,23]

Table 1. Relaxivities of various MnO-based nanostructures.

	Relaxivity ($\text{mM}^{-1} \text{ s}^{-1}$, [Mn])		
	r_1	r_2	r_2/r_1
CADMO-7	5.42	31.32	5.78
CADMO-17	1.91	11.59	6.07
EnMO-7	0.35	1.74	4.97
EnMO-17	0.18	0.52	2.88
HMON ^[14]	1.42 ^[11]	7.74	5.45
MONP ^[15]	1.97 ^[12]	n.a. ^[a]	n.a. ^[a]

[a] n.a.: not available.

The cytotoxicity of CADMO-7 and CADMO-17 against RAW 264.7 cells was assessed by using the WST-1 cellular proliferation assay based on mitochondrial oxidation (Figure 5). Cell viability was examined after incubation with CADMO-7 at concentrations ranging from 25 to $800 \mu\text{g mL}^{-1}$ for 24 h. The treated RAW 264.7 cells maintained over 90% cell viability at high CADMO concentrations (up to $800 \mu\text{g mL}^{-1}$), which indicates that CADMOs are biocompatible even at high nanoparticle concentrations.

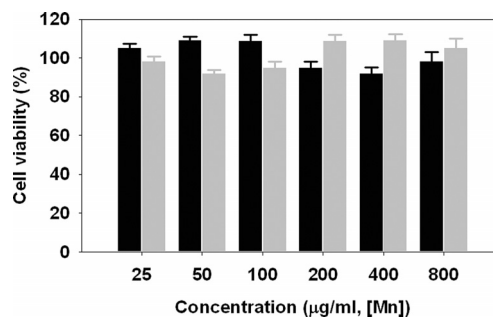


Figure 5. Cell viability test of CADMO-7 (black) and CADMO-17 (gray) by the WST-1 cellular proliferation assay.

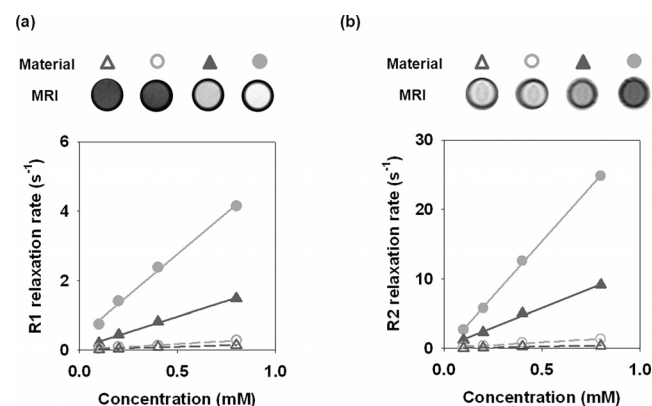


Figure 4. (a) T_1 -weighted MR images and plots of $1/T_1$ against Mn concentration. The slopes indicate the specific relaxivity (r_1). (b) T_2 -weighted MR images of MnO nanoparticles and plots of $1/T_2$ against Mn concentration. (●) CADMO-7, (▲) CADMO-17, (○) EnMO-7 and (△) EnMO-17.

To evaluate the potential of CADMOs in T_1 cellular imaging, RAW 264.7 cells treated with EnMO-7, EnMO-17, CADMO-7 and CADMO-17 were compared with non-treated cells. RAW 264.7 cell lines are well known as the monocyte macrophage cell line derived from BALB/c mice. RAW 264.7 cells treated with CADMO-7 showed an approximately 296% higher T_1 signal with a bright image relative to that of non-treated macrophage cells (Figure 6, a). Furthermore, CM-dextran-functionalized materials (CADMO-7 and CADMO-17) were more efficiently taken up than the encapsulated MnO nanoparticles (EnMO-7 and EnMO-17). This shows that CM-dextran plays an important role in the uptake by macrophage cells. The two dif-

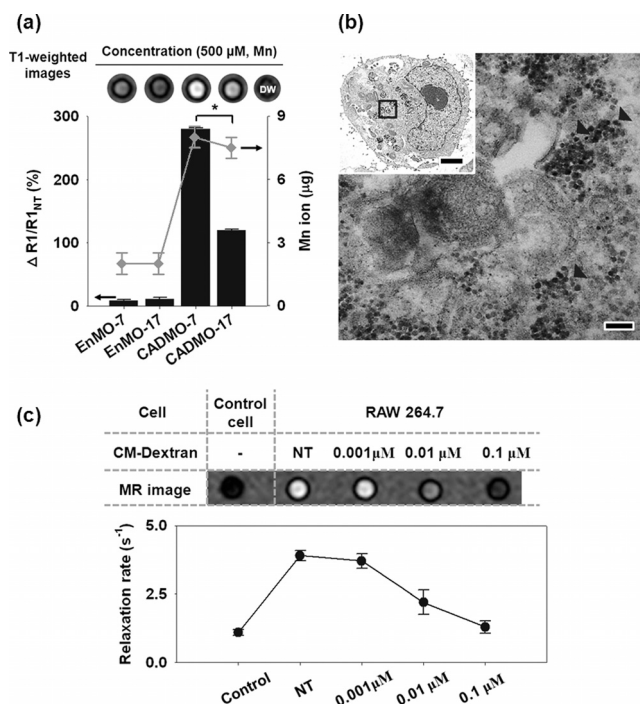


Figure 6. (a) T_1 -weighted MR images and relative signal intensity graphs of RAW 264.7 cells incubated with EnMO-7, EnMO-17, CADMO-7 and CADMO-17 at 500 μM for 6 h in buffer solution and their corresponding Mn concentrations determined by ICP-AES (*: $p < 0.05$). (b) TEM images (right; scale bar: 200 nm) of RAW 264.7 cells treated with CADMOs. Main image: scale bar: 200 nm; inset: scale bar: 2 μm . (c) CM-dextran concentration-dependent uptake efficiency of CADMOs. T_1 MR images of RAW264.7 cell line treated with CADMO-7 and relaxation rate graph of RAW 264.7 cells treated with CADMO-7 vs. various concentrations of CM-dextran after treatment. The relaxivity of the RAW 264.7 cell line is 1.029998 s^{-1} .

ferent sizes of CM-dextran-functionalized MnO nanoparticles (CADMO-7 and CADMO-17) were compared; CADMO-7 treated cells demonstrated a 2.9-fold higher signal intensity even though the Mn ions were present in similar concentrations. This suggests that the smaller-sized MnO nanoparticles, for example, CADMO-7, is a more desirable T_1 contrast agent with a higher surface-to-volume ratio. Furthermore, cellular TEM images show that CADMOs can be detected in RAW 264.7 cells (Figure 6, b). We also investigated the consequences of CM-dextran playing an important role in the uptake by measuring the binding affinity of CADMOs to RAW 264.7 cells using an inhibition test with CM-dextran. Before incubating CADMOs with RAW 264.7 cells, CM-dextran (molar ratio: 0.1, 1.0 and 10.0 μM) as a binding inhibitor was added to each well and left to stand for 1 h at 4 $^{\circ}\text{C}$. After washing away the unbound CM-dextran, CADMO-7 was added to each well. As the binding inhibition molar ratio of CM-dextran increased, the T_1 -weighted MR images for RAW 264.7 cells treated with CADMO-7 gradually changed from bright white to dark black (Figure 6, c). Consequently, we believe that these results prove that CM-dextran plays an important role in the uptake by macrophage cells.^[24–26]

As a proof of concept, MRI experiments were performed to demonstrate the excellent T_1 contrast ability of CADMO-7 in vivo. MR images were obtained before and after the intravenous injection of CADMO-7 (800 $\mu\text{g}/\text{Mn}$). In balb/c nude mice (aged six weeks), we readily detected an enhanced liver signal in vivo in a series of 1.5T MR images taken with clinical MRI equipment (Figure 7, a). The contrast agents in liver were enhanced initially and maintained for around 4 h. We next evaluated their biodistributions by using T_1 -weighted MR images. The mice were sacrificed 4 h after the injection and their livers were collected and subjected to an ex vivo MRI scan plate for comparison with non-treated mice organs (Figure 7, b). Ex vivo T_1 MR images of the excised livers provided substantial additional evidence for an enhanced longitudinal relaxation rate (bright image) compared with the non-treated liver image. In addition, the relative Mn concentrations of distributed CADMO-7 were compared with those of non-treated mouse in different organs ($\Delta C = C - C_{NT}$, NT = non-treated). CADMO-7 was detected mainly in liver tissue, and the uptakes in normal tissues were not significant providing decisive evidence that CADMO-7 specifically accumulates in liver tissues (Figure 7, c). In addition, the strong signal in the kidney tissue is due to the excretion of CADMO-7, indicative of the clearance that is a prerequisite for clinical applications. Consequently, the results demonstrate the potential of CADMO-7 as a T_1 contrast agent for diagnostic and clinical applications.

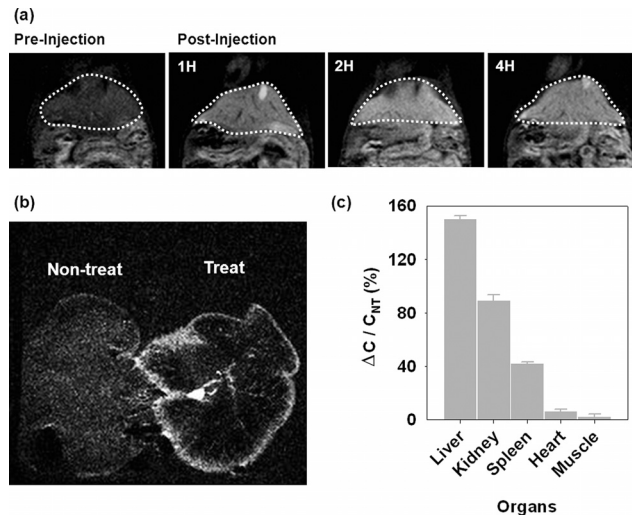


Figure 7. (a) In vivo MR images of nude mice after intravenous injection of CADMO-7 (800 μg Mn per mouse) at different times (pre-injection, 1, 2 and 4 h), (b) T_1 -weighted ex vivo MR images of liver and (c) relative concentrations of CADMOs (Mn ions) in mice treated with CADMO-7 vs. those in non-treated mice groups (NT).

Conclusions

We have synthesized carboxymethyl-dextran-functionalized MnO (CADMO) nanoparticles for use as a T_1 magnetic resonance imaging contrast agent. The hydrophobic MnO nanoparticles could successfully undergo phase trans-

fer into the aqueous phase by introducing biocompatible and hydrophilic CM-dextran by a robust ligand exchange method. Moreover, nanoparticle core surfaces were exposed to excited water molecules and exhibit a strongly enhanced r_1 relaxivity ($5.42 \text{ mM}^{-1} \text{ s}^{-1}$). Furthermore, efficient targeting with the excellent ligand binding capacity provided by the CM-dextran coating makes CADMOs promising contrast agents for targeted imaging of the liver or inflammatory macrophage cells. In addition, we envisage that this study may provide a potential T_1 contrast agent with enhanced ability for future clinical trials.

Experimental Section

General: Diethylene glycol (DEG), manganese(II) acetylacetonate [$\text{Mn}(\text{acac})_2$], oleylamine (70%) and CM-dextran were purchased from Sigma-Aldrich. Ethyl alcohol (denatured) and toluene (99.8%) were obtained from Samchun Chemical. 1-Ethyl-3-[3-(dimethylamino)propyl]carbodiimide hydrochloride (EDC) and *N*-hydroxysuccinimide (NHS) were purchased from Pierce. Cy5.5 dye was purchased from GE healthcare. Oleylamine was purified by vacuum distillation over CaH_2 . All other reagents purchased from commercial sources were used as obtained without further purification. Ultrapure deionized water was used for all of the synthetic processes.

Synthesis of MnO Nanoparticles (7 nm): A slurry of $\text{Mn}(\text{acac})_2$ (0.30 g, 1.19 mmol), oleylamine (7.61 g, 28.44 mmol) and H_2O (0.21 g, 11.85 mmol) in a 100 mL Schlenk flask equipped with a condenser, which was connected to a bubbler, was heated at 150°C for 9 h. The resulting reaction mixture was cooled to room temperature to form a brown suspension and the resulting solution was added to excess ethanol (20 mL). Precipitates were formed, which were then isolated by centrifugation at 6000 rpm for 10 min. Oleylamine-capped MnO nanoparticles were obtained as a brown powder, which could be easily re-dispersed into various organic solvents, for example, hexane, toluene and dichloromethane.

Synthesis of MnO Nanoparticles (17 nm): A slurry of $\text{Mn}(\text{acac})_2$ (0.30 g, 1.19 mmol), oleylamine (7.61 g, 28.44 mmol) and H_2O (0.21 g, 11.85 mmol) in a 100 mL Schlenk flask equipped with a condenser, which was connected to a bubbler, was heated at 250°C for 9 h. The rest of the procedure was as described above for the formation of the 7 nm nanoparticles.

Preparation of Carboxymethyl-Dextran MnO Nanoparticles: A DEG solution (10.0 mL) of CM-dextran (100 mg) was first heated to 220°C with vigorous stirring under N_2 . A solution of toluene containing MnO nanocrystals (10 mg/mL) was then injected into the DEG/CM-dextran solution and the turbidity of the mixture was immediately observed. Subsequently, the system was heated to 250°C and held there for 1 h until the solution became clear. After cooling the solution to room temperature, ethanol (20 mL) was added and a brown-black powder was ultimately obtained after centrifugation. The product was further purified by centrifugal filter (Centriprep, 20 kDa NMWL, Amicon) with two cycles at 1000g force for 0.5 h.

Preparation of Near-Infrared Fluorescence Carboxymethyl-Dextran MnO Nanoparticles: For the further functionalization of CADMO-7 with fluorophores using the available carboxylic ester groups of CM-dextran, a solution (1.2 mL) containing diluted CADMO was mixed with EDC (1 mmol) with vigorous stirring. After 30 min of activation, NHS sodium salt (1 mmol) was added to the suspen-

sion. After stirring for 1.5 h, the suspension was added dropwise to amine-functionalized Cy5.5 (6.16 μL) in buffer (1.0 mL) at pH 7.4. The solution was vigorously mixed for 24 h at room temperature and was then subjected to dialysis against Millipore water in a dialysis membrane (Spectra/Por® 4 Regenerated Cellulose Membrane, MWCO = 20 K) over 48 h to remove unreacted components. Light exposure was minimized to prevent possible photobleaching during the experiment. Further purification was achieved with a Centriprep device (3000g force, 30 min) by removing the top of the suspension and resuspending the remainder in the Centriprep filter. This cycle was repeated twice until the supernatant failed to yield a fluorescent signal.

Assessment of In Vitro Cell Viability: Cell viability was quantified with a colorimetric assay based on a tetrazolium salt (WST-1) using a cell proliferation kit (Takara Bio Inc., Japan). Succinate tetrazolium reductase exists in the mitochondrial respiratory chain and is only active in viable cells, cleaving the tetrazolium salt (WST-1) into soluble formazan dye. RAW 264.7 cells were obtained from the American Type Culture Collection (ATCC, USA) and the cells were plated at a density of 4×10^5 cells/100 μL in a 96-well plate and incubated at 37°C under a 5% CO_2 atmosphere. The cells were incubated for 24 h with CADMO-7 (100 μL) at high concentrations (400 $\mu\text{g/mL}$) and then rinsed with PBS (pH 7.4, 100 μL , 1 mM). The cells were then added to minimum essential media (100 μL) supplemented with 10% fetal bovine serum (FBS), 1% antibiotic antimycotic and non-essential amino acids (Gibco®, Invitrogen, USA) and treated with freshly prepared tetrazolium salt (10 μL). After 2 h, the plate was assayed by using an enzyme-linked immunosorbent assay (Spectra MAX 340, Molecular Devices, USA) at an absorbance wavelength of 450 nm and a reference wavelength of 650 nm.

Cellular Imaging: A solution of 2×10^6 RAW 264.7 cells suspended in PBS (1 mL) was mixed with CADMO-7 (120 μL) and incubated. MRI scans of in vitro cell phantoms were obtained by using a 1.5T clinical MRI instrument with a micro-47 surface coil (Intera, Philips Medical Systems, Best, The Netherlands). For the acquisition of T_1 -weighted MR images of CADMO-7, the following parameters were adopted: resolution: $234 \times 234 \mu\text{m}$, section thickness: 3.0 mm, TE = 18 ms, TR = 625 ms and number of acquisitions: 2. For the cellular TEM sample preparation, RAW 264.7 cells (3×10^5 cells/mL) were seeded into six-well plates for 24 h. The RAW 264.7 cells were rinsed with PBS (pH 7.4, 1 mM) and CADMO-7 (10 μg of Mn/mL) and added to minimum essential media supplemented with 10% FBS and 1% antibiotic antimycotic and non-essential amino acid (Gibco®, Invitrogen, USA). After incubation for 12 h at 37°C , the cells with CADMO-7 were trypsinized, centrifuged and washed three times with blocking buffer (0.03% bovine serum albumin and 0.01% NaN_3 in PBS). Then the samples were fixed according to the standard fixation and embedding protocol for resin section TEM. The sections were then cut by using a LEICA Ultracut UCT Ultramicrotome (Leica Microsystems, Austria). All of the samples were observed by TEM (JEM-1011, JEOL, Japan) at an acceleration voltage of 80 kV.

Animal MR Imaging: We performed in vitro and in vivo MR imaging experiments with a 1.5T clinical MRI instrument with a micro-47 surface coil (Intera, Philips Medical Systems, Best, Netherlands). For the acquisition of T_1 -weighted MR images of CADMO-7, the following parameters were adopted: resolution: $234 \times 234 \mu\text{m}$, section thickness: 3.0 mm, TE = 18 ms, TR = 625 ms and number of acquisitions: 2. The relaxivity coefficient ($\text{mM}^{-1} \text{ s}^{-1}$) was equal to the ratio of the R_1 ($1/T_1$ [s^{-1}]) to Mn concentration.

Ex Vivo Optical Imaging: NIR fluorescence images were obtained with an eXplore Optix system (ART Advanced Research Technol-

ogies Inc., Montreal, Canada). Imaging was performed for excised organs 2 h after injection of CADMO-7 and images were assessed with an Analysis Workstation (ART Advanced Research Technologies Inc.). Laser power and count time settings were optimized at 10 μ W and 0.1 s per point, respectively. Excitation and emission spots were raster-scanned in 1 mm steps over the selected region of interest to generate emission wavelength scans. A 670 nm pulsed laser diode was applied to excite the Cy5.5 molecules. NIR fluorescence emissions at 700 nm were collected, including whole organs and 2D slice images, and were calculated by using the region of interest (ROI) function of the Analysis Workstation software.

Supporting Information (see footnote on the first page of this article): Characterization data for compounds; TEM image, additional solubility test image, stability test in serum, calculation of the total surface area and relaxation properties, T_1 -weighted MR images, ex vivo NIR fluorescence images.

Acknowledgments

This study was supported by a grant from the Korea Health 21 R&D Project, the Ministry of Health and Welfare, the Republic of Korea (A085136).

- [1] E. C. Cho, J. Xie, P. A. Wurm, Y. Xia, *Nano Lett.* **2009**, *9*, 1080–1084.
- [2] S. Tong, S. Hou, Z. Zheng, J. Zhou, G. Bao, *Nano Lett.* **2010**, *10*, 4607–4613.
- [3] A. Verma, O. Uzun, Y. Hu, Y. Hu, H.-S. Han, N. Watson, S. Chen, D. J. Irvine, F. Stellacci, *Nat. Mater.* **2008**, *7*, 588–595.
- [4] C. M. Jewell, J.-M. Jung, P. U. Atukorale, R. P. Carney, F. Stellacci, D. J. Irvine, *Angew. Chem. Int. Ed.* **2011**, *50*, 12312–12315.
- [5] J. Shin, R. M. Anisur, M. K. Ko, G. H. Im, J. H. Lee, I. S. Lee, *Angew. Chem.* **2009**, *121*, 327; *Angew. Chem. Int. Ed.* **2009**, *48*, 321–324.
- [6] J. Huang, J. Xie, K. Chen, L. Bu, S. Lee, Z. Cheng, X. Li, X. Chen, *Chem. Commun.* **2010**, *46*, 6684–6686.
- [7] J.-o. Deguchi, M. Aikawa, C.-H. Tung, E. Aikawa, D.-E. Kim, V. Ntziachristos, R. Weissleder, P. Libby, *Circulation* **2006**, *114*, 55–62.
- [8] A. N. Pande, R. H. Kohler, E. Aikawa, R. Weissleder, F. A. Jaffer, *J. Biomed. Opt.* **2006**, *11*, 021009–021007.
- [9] V. Amirbekian, M. J. Lipinski, K. C. Briley-Saebo, S. Amirbekian, J. G. S. Aguinaldo, D. B. Weinreb, E. Vucic, J. C. Frias, F. Hyafil, V. Mani, E. A. Fisher, Z. A. Fayad, *Proc. Natl. Acad. Sci. USA* **2007**, *104*, 961–966.
- [10] R. L. Tiwari, V. Singh, M. K. Barthwal, *Med. Res. Rev.* **2008**, *28*, 483–544.
- [11] L. Tong, J.-X. Cheng, *Nanomedicine* **2009**, *4*, 265–276.
- [12] F. A. Jaffer, P. Libby, R. Weissleder, *Circulation* **2007**, *116*, 1052–1061.
- [13] J. Sanz, Z. A. Fayad, *Nature* **2008**, *451*, 953–957.
- [14] E.-K. Lim, E. Jang, B. Kim, J. Choi, K. Lee, J.-S. Suh, Y.-M. Huh, S. Haam, *J. Mater. Chem.* **2011**, *21*, 12473.
- [15] R. Choi, J. Yang, J. Choi, E. K. Lim, E. Kim, J. S. Suh, Y. M. Huh, S. Haam, *Langmuir: ACS J. Surf. Colloids* **2010**, *26*, 17520–17527.
- [16] W. S. Seo, H. H. Jo, K. Lee, B. Kim, S. J. Oh, J. T. Park, *Angew. Chem.* **2004**, *116*, 1135–1137.
- [17] T. Zhang, J. Ge, Y. Hu, Y. Yin, *Nano Lett.* **2007**, *7*, 3203–3207.
- [18] M. J. Baek, J. Y. Park, W. Xu, K. Kattel, H. G. Kim, E. J. Lee, A. K. Patel, J. J. Lee, Y. Chang, T. J. Kim, J. E. Bae, K. S. Chae, G. H. Lee, *ACS Appl. Mater. Interfaces* **2010**, *2*, 2949–2955.
- [19] J. Y. Park, M. J. Baek, E. S. Choi, S. Woo, J. H. Kim, T. J. Kim, J. C. Jung, K. S. Chae, Y. Chang, G. H. Lee, *ACS Nano* **2009**, *3*, 3663–3669.
- [20] C. C. Huang, N. H. Khu, C. S. Yeh, *Biomaterials* **2010**, *31*, 4073–4078.
- [21] D. Pan, A. Senpan, S. D. Caruthers, T. A. Williams, M. J. Scott, P. J. Gaffney, S. A. Wickline, G. M. Lanza, *Chem. Commun.* **2009**, 3234–3236.
- [22] P. Gillis, F. Moyn, R. A. Brooks, *Magn. Reson. Med.* **2002**, *47*, 257–263.
- [23] R. A. Brooks, F. Moyn, P. Gillis, *Magn. Reson. Med.* **2001**, *45*, 1014–1020.
- [24] T. Matsushita, Y. Kusakabe, H. Fujii, K. Murase, Y. Yamazaki, K. Murse, *Magn. Reson. Med.* **2011**, *29*, 173–179.
- [25] N. Beckman, C. Cannet, M. Fringeli-Taanner, D. Baumann, C. Pally, C. Bruns, H.-G. Zerwes, E. Andriambeloson, M. Bigaud, *Magn. Reson. Med.* **2003**, *49*, 459–456.
- [26] M. E. Kooi, V. C. Cappendijk, K. B. J. M. Cleutjens, A. G. H. Kessels, P. J. E. H. M. Kitslaar, M. Borgers, P. M. Frederik, M. J. A. P. Daemen, J. M. A. van Engelshoven, *Circulation* **2003**, *107*, 2453–2487.

Received: September 6, 2012

Published Online: October 30, 2012